Gate-controlled topological conducting channels in bilayer graphene

Jing Li[1], Ke Wang[2,3], Kenton J. McFaul[4], Zachary Zern[1], Yafei Ren[2,3], Kenji Watanabe[5], Takashi Taniguchi[5], Zhenhua Qiao[2,3]★ and Jun Zhu[1,6]★

The existence of inequivalent valleys K and K′ in the momentum space of 2D hexagonal lattices provides a new electronic degree of freedom, the manipulation of which can potentially lead to new types of electronics, analogous to the role played by electron spin[1-3]. In materials with broken inversion symmetry, such as an electrically gated bilayer graphene (BLG)[4,5], the momentum-space Berry curvature Ω carries opposite sign in the K and K′ valleys. A sign reversal of Ω along an internal boundary of the sheet gives rise to counterpropagating 1D conducting modes encoded with opposite-valley indices. These metallic states are topologically protected against backscattering in the absence of valley-mixing scattering, and thus can carry current ballistically[1,6-11]. In BLG, the reversal of Ω can occur at the domain wall of AB- and BA-stacked domains[12-14], or at the line junction of two oppositely gated regions[6]. The latter approach can provide a scalable platform to implement valleytronic operations, such as valves and waveguides[9,15], but it is technically challenging to realize. Here, we fabricate a dual-split-gate structure in BLG and present evidence of the predicted metallic states in electrical transport. The metallic states possess a mean free path (MFP) of up to a few hundred nanometres in the absence of a magnetic field. The application of a perpendicular magnetic field suppresses the backscattering significantly and enables a junction 400 nm in length to exhibit conductance close to the ballistic limit of $4e^2/h$ at 8 T. Our experiment paves the way to the realization of gate-controlled ballistic valley transport and the development of valleytronic applications in atomically thin materials.

Exploiting the valley degree of freedom in hexagonal lattices may offer an alternative pathway to achieving electronics of low power consumption. Experiments have shown that a net valley polarization in the material can be induced by the use of circularly polarized light[2,16,17] or a net bulk current[18–20]. However, the use of light is not always desirable in electronics and device proposals using bulk valley polarization often put stringent requirements on the size and edge orientation of the active area[3]. Alternatively, electrically created, valley-polarized topological conducting channels in high-mobility BLG may offer a robust, scalable platform to realize valley-tronic operations[1,6,8–15]. Figure 1a illustrates the dual-split-gating scheme proposed by Martin et al.[6], in which an AB-stacked BLG sheet is controlled by two pairs of top and bottom gates separated by a line junction. The device operates in the regime in which both the left and the right regions of the BLG sheet are insulating because of a bulk bandgap induced by the independently applied
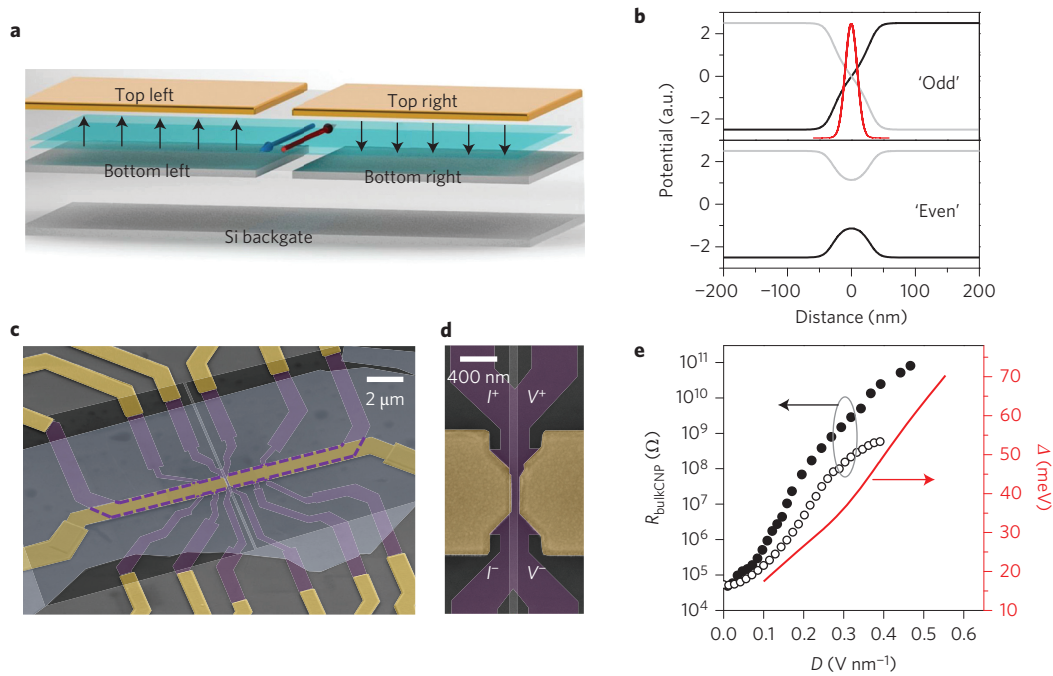
displacement fields D_L and D_R. In the 'odd' field configuration, where $D_L D_R < 0$, theory predicts the existence of eight conducting modes (referred to as the 'kink' states) that propagate along the line of interlayer electrostatic potential difference, $V = 0$ (see Supplementary Section 1 for simulations). Each valley supports four chiral modes (two resulting from spin degeneracy and two resulting from layer number) with modes from different valleys counterpropagating, as illustrated in Fig. 1a. Their wavefunctions overlap in real space (Fig. 1b), but are orthogonal in the absence of short-range disorder. In such cases, backscattering is forbidden and the junction is expected to exhibit a quantized conductance of $4e^2/h$. In comparison, in the 'even' field configuration, that is, $D_L D_R > 0$, the junction is expected to be insulating as no kink state is present. This sharp contrast thus enables a clear and convincing demonstration of the existence of the kink states.

The above proposal poses a number of fabrication challenges, which include the precise alignment of the four split gates shown in Fig. 1a and the necessity of hexagonal boron nitride (h-BN) encapsulation to achieve the high sample quality needed to suppress subgap conduction caused by disorder[5,21]. In this work, we have overcome these obstacles and present experimental evidence of the kink states. The devices are made by sequentially stacking h-BN, BLG and h-BN atop multilayer graphene split-bottom gates supported on a SiO$_2$/doped Si substrate[22]. The fabrication and alignment procedures are detailed in the Methods and Supplementary Section 2. A false-colour scanning electron micrograph (SEM) image of a finished device is shown in Fig. 1c, with the junction area highlighted in Fig. 1d. We can align the top and bottom splits to better than 10 nm in general. The results reported here are based on two devices. Their junction widths w and lengths L are $w = 70$ nm and $L = 1$ μm for device 1 and $w = 110$ nm and $L = 400$ nm for device 2. Measurements of the bulk regions yield high carrier mobilities, μ, of 100,000 cm^2 V^{-1} s^{-1} and 22,000 cm^2 V^{-1} s^{-1}, respectively, for devices 1 and 2, in comparison with μ of a few 1,000 cm^2 V^{-1} s^{-1} on oxide-supported samples[5]. The characteristics of the devices and the measurement techniques are described in detail in Supplementary Section 3. Measurements are performed at $T = 1.6$ K unless otherwise noted.

The high quality of the devices ensures insulating behaviour of the bulk BLG when the Fermi level, E_F, resides inside the bulk bandgap Δ, which is a few tens of millielectronvolts in our experiment. This is evident from the plot of the bulk charge-neutrality point (CNP) resistance, $R_{bulkCNP}$, versus the displacement field D (Fig. 1e). It is more than 10 MΩ in the D-field range of our

[1]Department of Physics, The Pennsylvania State University, University Park, Pennsylvania 16802, USA. [2]ICQD, Hefei National Laboratory for Physical Sciences at Microscale, and Synergetic Innovation Center of Quantum Information and Quantum Physics, University of Science and Technology of China, Hefei, Anhui 230026, China. [3]CAS Key Laboratory of Strongly-Coupled Quantum Matter Physics, and Department of Physics, University of Science and Technology of China, Hefei, Anhui 230026, China. [4]Department of Electrical Engineering, Grove City College, Grove City, Pennsylvania 16127, USA. [5]National Institute for Material Science, 1-1 Namiki, Tsukuba 305-0044, Japan. [6]Center for 2-Dimensional and Layered Materials, The Pennsylvania State University, University Park, Pennsylvania 16802, USA. *e-mail: jzhu@phys.psu.edu; qiao@ustc.edu.cn

Figure 1 | Device structure and characterization. a, Schematic of our dual-split-gated BLG device. The four split gates independently control the bulk displacement fields D_L and D_R on the left and right sides of the junction. The Si backgate tunes E_F of the line junction. The gating efficiencies of the split gates are determined using the quantum Hall effect. We determined the gate voltages that correspond to the $D = 0$ and $n = 0$ state on the left and right sides of the junction using the global minima of $R_{bulkCNP}$. Subsequent measurements were done at $n_L = n_R = 0$ and constant displacement fields D_L and D_R. The diagram shows the odd-field configuration that results in the presence of the helical kink states at the line junction. Blue and red arrows correspond to modes that carry valley indexes K and K', respectively. Each one contains four modes to account for the spin and layer degeneracy. **b**, External electrostatic potential profile near the top (grey) and bottom (black) graphene layers for the configurations of the odd ($D_L D_R < 0$) and even ($D_L D_R > 0$) fields. Potential simulations are performed using the COMSOL package and parameters of device 1. The crossing of the potentials at $V = 0$ gives rise to the topological kink states. The red curve plots the wavefunction distribution of one such state schematically, with a full-width at half-maximum of 22 nm. **c**, A false-colour SEM image of a device similar to device 2. The BLG is shaded and outlined in purple, the top gates and electrodes are gold, the bottom multilayer graphene split gates are black and the top h-BN dielectric layer is grey. The bottom h-BN layer extends beyond the entire image. **d**, A close-up view of the junction area from another device similar to device 2. The junction is connected to four BLG electrodes and the measurements use a quasi-four-terminal geometry, as shown in the image, to eliminate the electrode resistance. Alignment of the gates is generally better than 10 nm. **e**, $R_{bulkCNP}$ as a function of the applied displacement field D for devices 1 (filled symbols) and 2 (open symbols) in a semilog plot (left axis). Supplementary Fig. 5 gives the device schematic and electrodes used in the measurements. $R_{bulkCNP}$ rises much more rapidly with the increase of D compared with that of oxide-supported samples and is larger than 10 MΩ in the range of measurements below. Also plotted on the right is the D-dependent bulk bandgap Δ obtained from temperature-dependence measurements of a device similar to device 2 (ref. 34).

measurements, which renders its contribution to the measured junction conductance negligible.

Figure 2 presents the experimental observations of the kink states in device 1. We measured the junction conductance $\sigma_j = 1/R_j$ (R_j, junction resistance) as a function of the silicon backgate voltage V_{Si}, which controls E_F in the junction, at a series of fixed D_L and D_R values of both polarities. As an example, in Fig. 2a σ_j is plotted as functions of D_R and V_{Si} at $D_L = -0.25$ V nm^{-1} (upper panel) and $+0.25$ V nm^{-1} (lower panel). The diagonal features that connect the lower-left to the upper-right corners of the panels correspond to the charge-neutrality region of the line junction, whose dependence on D_R and D_L is attributed to a slight misalignment between the top and bottom gates (Supplementary Section 4). It is immediately clear from the data that σ_j near the CNP of the junction is high in the odd-field configuration (in white), but low in the even-field configuration (in blue). This difference is illustrated further in Fig. 2b, in which we plot σ_j cut along the two yellow dashed lines drawn in Fig. 2a; σ_j is high in both configurations when E_F is outside the bulk bandgap. However, when E_F is inside the bandgap, σ_j decreases to less than 1 µS in the even configuration, but remains high, in the range of 10–15 µS, in the odd configuration, which indicates the presence of additional conducting channels. Such disparate behaviour of σ_j in the even- and

odd-field configurations is observed systematically. To illustrate this contrast, we plot in Fig. 2c R_j at the CNP of the junction only, taking data from many panels similar to that shown in Fig. 2a and spanning all four polarity combinations of D_L and D_R. The clear contrast between the even, that is, $(+ +)$ and $(- -)$, and the odd, that is, $(+ -)$ and $(- +)$, quadrants of the graph strongly supports the existence of the kink states in the odd-field configuration, as expected from theory[6].

In general, R_j of the kink states ranges from 40 to 100 kΩ, which corresponds to a MFP of $L_k = 70$–200 nm using the Landauer–Büttiker formula:

$$R_j = R_0(1 + L/L_k) \tag{1}$$

where $R_0 = h/4e^2 = 6.5$ kΩ is the ballistic resistance limit of the fourfold degenerate kink states and $L = 1$ µm is the junction length in device 1 (ref. 23). Although a small contact resistance (several kiloohms) may originate from the electrode/kink interface (Supplementary Section 5), the large value of R_j indicates significant backscattering, that is, intervalley mixing of the kink states. A MFP of $L_k < 200$ nm is surprisingly short, given that the bulk 2D MFP, L_{2D}, in our high-quality devices is also a few hundred nanometres. Intuitively and experimentally[14], one expects $L_k \gg L_{2D}$ because L_{2D} is dominated
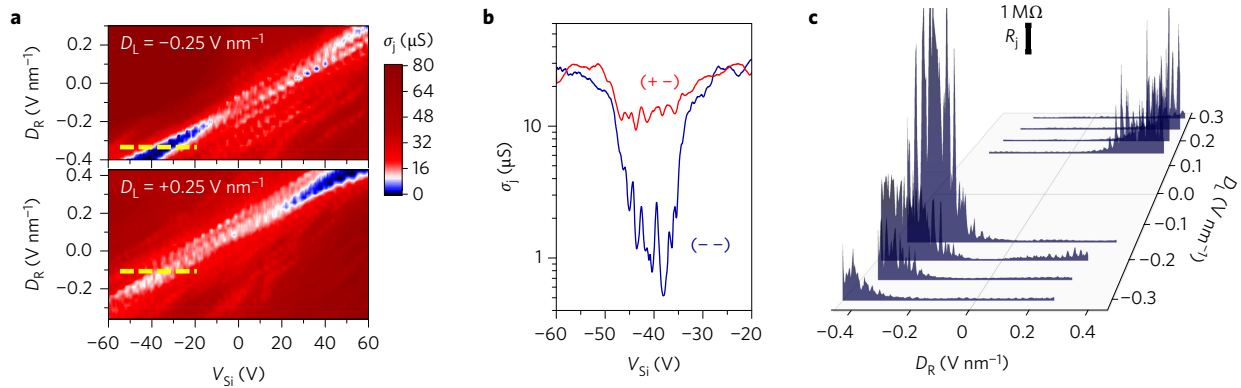
Figure 2 | Evidences of kink states. a, The junction conductance σ_j as a function of V_{Si} at fixed values of D_R from −0.4 to 0.4 V nm^{-1} (from device 1). Upper panel: $D_L = -0.25$ V nm^{-1}. Lower panel: $D_L = +0.25$ V nm^{-1}. The diagonal bands in the plots correspond to the CNP of the line junction. **b**, σ_j versus V_{Si} along the yellow dashed lines marked in the upper (blue curve) and lower (red curve) panels of **a**. We estimate that the energy range of the bulk bandgap Δ here corresponds to roughly 25 V on V_{Si}. The presence of the kink states in the (+ −)-field configuration (red curve) gives rise to high conductance inside the bandgap, whereas σ_j is low in the (− −)-field configuration (blue curve). **c**, R_j at the CNP of the junction as a function of D_L and D_R in all four field polarities shows systematically high resistances in the even configurations and low resistances in the odd configurations.
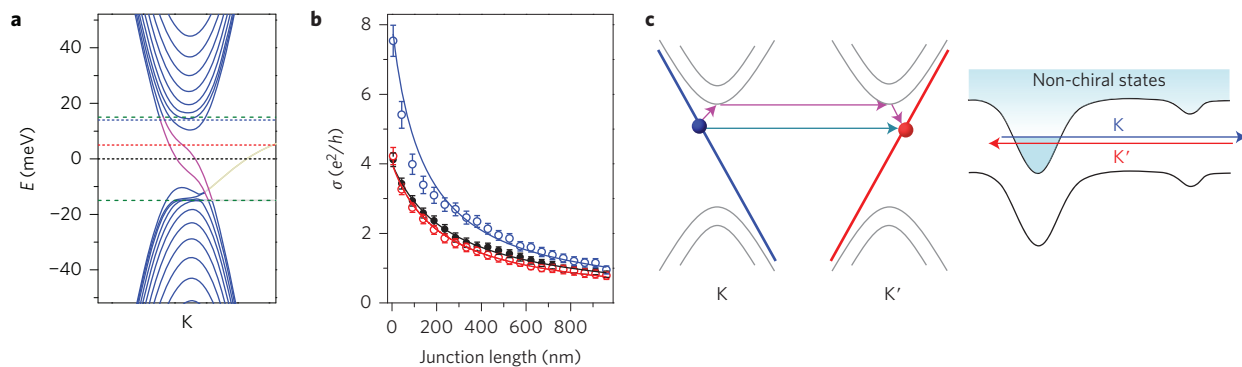

Figure 3 | Calculated band structure and conductance of the kink states. a, Band structures of the junction in device 1 ($w = 70$ nm) calculated using the COMSOL-simulated potential profiles shown in Fig. 1b. Only the K valley is shown. Non-chiral states bound at the junction reside inside the bulk bandgap marked by the green dashed lines ($\Delta = 30$ meV). The kink states are shown in magenta. The grey line corresponds to edge states at the zigzag boundary of the numerical set-up, which do not survive edge disorder in realistic samples. **b**, Junction conductance σ versus length L calculated at $E_F = 0$ (black), 5 (red) and 14 meV (blue) as marked by the dashed lines in **a**. The disorder strength is chosen to be $W = 0.6$ eV. One non-chiral state is assumed to contribute conductance $4e^2/h$ at $L = 0$. Over 30 samples are averaged for each data point. Error bars are smaller than the symbol size. Fits to equation (1) yield MFPs of 266, 223 and 141 nm, respectively. The proximity to non-chiral states leads to enhanced backscattering. **c**, An illustration of intervalley scattering between the kink states of K and K′ valleys. A kink state may be scattered directly to a different valley or scattered via coupling to non-chiral states. Non-chiral states can also form quantum dots because of Coulomb potential fluctuations and coexist with the kink states over a large energy range, as shown schematically.

by a small momentum transfer (intravalley scattering events caused by long-range Coulomb impurities), whereas backscattering between kink states of different valleys requires a large momentum transfer, which should occur much less frequently, especially in h-BN-encapsulated clean samples[24]. Lattice defects cannot account for our observations; their rare occurrence is confirmed by the high mobility of the BLG bulk and experimentally determined resonant impurity scattering amplitude[25]. The large wavefunction spread, as depicted in Fig. 1b, also renders the kink states rather insensitive to scattering by point defects[9].

Although the nature of the backscattering mechanisms remains to be understood, there are several potentially relevant aspects of our experiment. Band-structure calculations (Supplementary Section 7) show that a smoothly varying electrostatic potential profile, such as the one we realized (see Fig. 1b), supports, in addition to the kink states that are chiral in each valley, non-chiral states the energies of which protrude into the bulk bandgap Δ, as shown in Fig. 3a[9,10]. These states are bound by the width of the junction but delocalized along its length. Their presence effectively reduces the size of the

bulk gap Δ, which is only a few tens of millielectronvolts in our experiment. Coulomb-disorder potential, as well as geometrical variations of the lithographically defined junction, can cause additional local variations of the energy of the non-chiral states, which results in their coexistence with the kink states within a larger energy range than suggested by band-structure calculations. At energies close to the CNP of the junction, the non-chiral states can potentially exist in the form of quantum dots. As illustrated in Fig. 3c, the coexisting non-chiral states can potentially enable kink states from different valleys to mix via multiple-particle processes, and thus introduce backscattering. Indeed, several such mechanisms have been put forward to explain the imprecise conductance quantization of the quantum-spin Hall edge states[26], including the possibility of a Kondo effect[27–30]. Similar mechanisms may be of relevance here and will be the subject of future studies. Furthermore, quantum dots formed by non-chiral states can also provide an explanation for the oscillations seen in the σ_j traces shown in Fig. 2b and for their I–V characteristics and temperature dependence, which we show and discuss in detail in Supplementary Section 6.
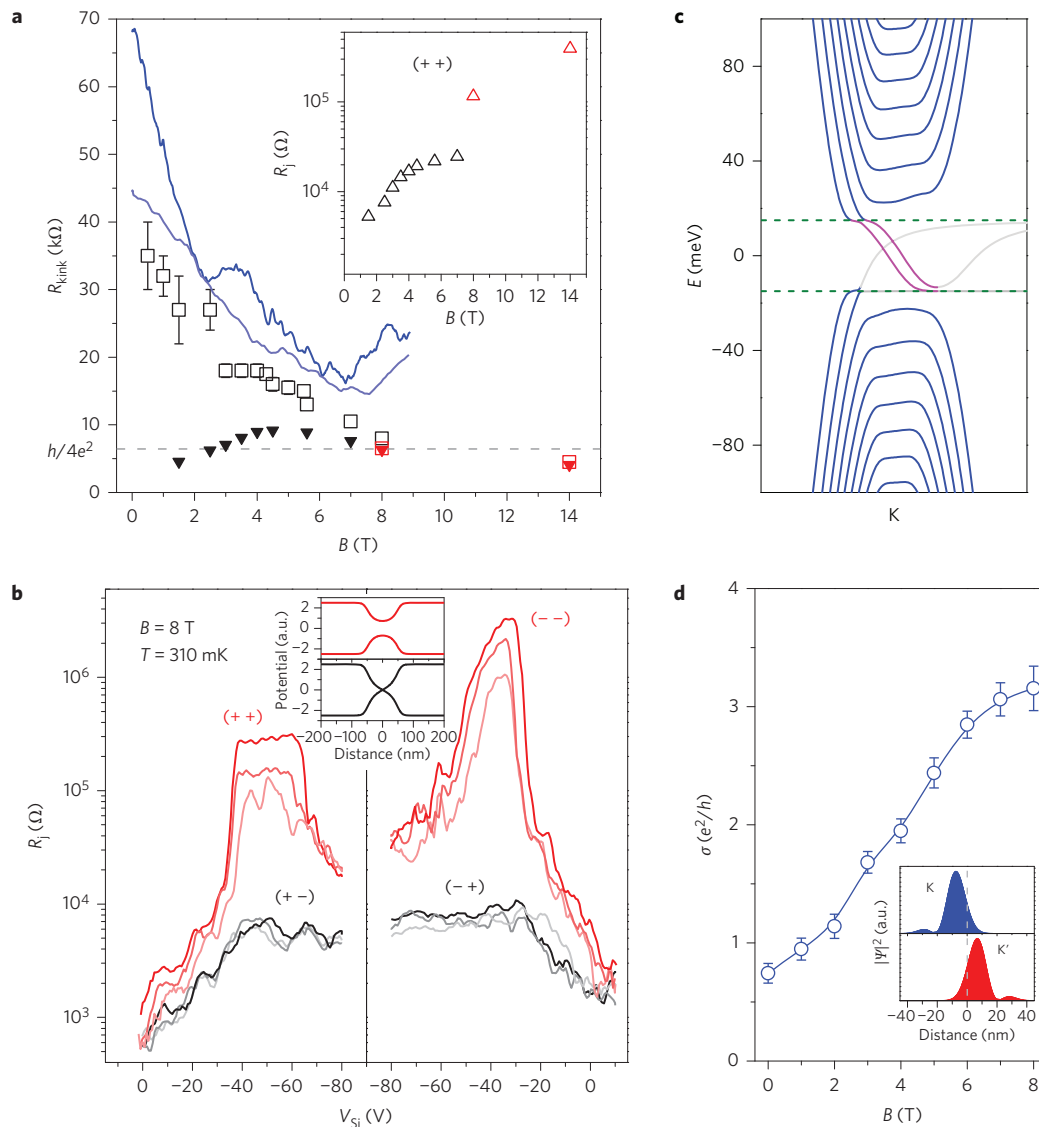
Figure 4 | Kink-state resistance in a magnetic field. a, Two representative magnetoresistance traces from device 1. D_L = +0.2 V nm^{-1} and D_R = −0.3 V nm^{-1}, and V_{Si} = −55.5 V and −39.3 V for the blue and light blue curves, respectively (Supplementary Section 10 gives the details of the measurements). Symbols are from device 2. The solid triangles are raw magnetoresistance data of R_j in the (+ −)-field configuration. R_j can be smaller than $h/4e^2$ because of a parallel conduction of the non-chiral states. We used a two-channel model to estimate the resistance of the kink states, using R_j of the (+ +)-field configuration shown in the inset to approximate the resistance of the parallel channel. The open squares plot the estimated resistance of the kink states. At a large magnetic field, the non-chiral states become sufficiently insulating that the raw R_j measures directly the kink-state resistance. Band-structure calculations and detailed discussions regarding the two-channel model are given in Supplementary Section 10. Black symbols, T = 1.6 K; red symbols, T = 310 mK in a separate cool down. $|D_L| = |D_R|$ = 0.3 V nm^{-1}. **b**, R_j versus V_{Si} in device 2 at B = 8 T for all four field configurations, as marked in the plot. From dark to light colours, $|D_L| = |D_R|$ = 0.5, 0.4 and 0.3 V nm^{-1}. Inset: potential profile for even (red)- and odd (black)-field configurations. **c**, The band structure of device 1 shown in Fig. 3a recalculated at B = 6 T. The olive dashed lines mark the edges of the bulk conduction and valance bands in Fig. 3a. Non-chiral states that reside below the band edges are now lifted to higher energies. The kink states are shown in magenta and the zigzag edge states are in grey (not relevant in realistic samples). **d**, The calculated magnetoconductance for device 1 (see Fig. 3b for the parameters used in the calculation). E_F = 5 meV. Inset: wavefunctions of the K (blue) and K′ (red) valley kink states at B = 6 T show a spatial separation of 14 nm caused by the Lorentz force. The wavefunction separation is zero at E_F = 0 and increases with increasing E_F; it also increases with increasing B (Supplementary Section 8 gives further details).

We performed numerical studies of the junction conductance using the Landauer–Büttiker formula and Green's function method (Supplementary Section 8) with on-site Anderson disorder in the energy range (−$W/2$, $W/2$), where W measures the disorder strength. Although the Anderson disorder may not reflect all the potential valley-mixing mechanisms in experimental samples, it provides an efficient means to model the conductance loss from intervalley scattering and allows us to examine the effect of the controlling factors of the experiment, such as the junction width w, the bulk gap size Δ and the E_F of the junction. A few key findings are

highlighted in Fig. 3, with the complete results given in Supplementary Section 8. The calculated band structure of device 1 with a bulk bandgap Δ = 30 meV is plotted in Fig. 3a. Δ is effectively reduced to ~21 meV because of the presence of the non-chiral states. Three length-dependent junction conductances $\sigma(L)$ that correspond to different Fermi levels, E_1 = 0, E_2 = 5 and E_3 = 14 meV (indicated by the dashed lines in Fig. 3a), are plotted in Fig. 3b. Fitting to equation (1) yields the MFP of the kink states, L_k = 266, 210 and 141 nm, respectively, for E_F = 0, 5 and 14 meV. We attribute the trend of decreasing conductance σ with

increasing E_F to the availability of more intervalley scattering paths that involve the non-chiral states as E_F moves towards, or resonates with, the energy of a non-chiral state. This situation is illustrated in Fig. 3c. Our calculations also show that L_k increases with increasing Δ and decreasing w, which points to effective ways of further improving the ballisticity of the kink states.

The application of a perpendicular magnetic field B effectively suppresses the backscattering process of the kink states. As Fig. 4a shows, the resistance of the kink states, R_{kink}, decreases rapidly with increasing B in both devices. R_{kink} reaches about 15 kΩ in device 1 at $B \approx 7$ T, which suggests an MFP of $L_k \approx 0.8$ μm. This is a factor of a 4–10 increase compared with L_k at $B = 0$ in this device. With a shorter junction length of 0.4 μm, R_{kink} of device 2 reaches and remains in the vicinity of the ballistic limit of $h/4e^2 = 6.5$ kΩ in the field range of 8–14 T. In Fig. 4b, we plot R_j versus V_{Si} of device 2 in all four displacement field polarities at $B = 8$ T. Near the CNP of the junction, R_j ranges approximately from 6 to 10 kΩ in the $(+ -)$- and $(- +)$-field configurations. R_j is also insensitive to the magnitude of the displacement field, which varies from 0.3 to 0.5 V nm^{-1}. In stark contrast, resistances of hundreds to thousands of kiloohms are observed in the two even-field configurations. These observations are quite remarkable and clearly attest to the presence of nearly ballistic kink states in the expected gating configurations.

The observed magnetoresistance of the kink states is reproduced satisfactorily by our numerical studies, as shown in Fig. 4c,d (Supplementary Section 9). Two effects of the magnetic field may play important roles. As Fig. 4c shows, the formation of Landau levels lifts the non-chiral states away from the energy range of the kink states, which should reduce the probability of any backscattering processes mediated by non-chiral states, as discussed earlier. In addition, the magnetic field exerts a Lorentz force of opposite directions on the counterpropagating kink states, which causes their wavefunctions to separate in space. This separation does not occur at $E_F = 0$, but widens with increasing E_F and is more pronounced in a wide junction[10,31]. It also increases with increasing B and can reach a size comparable to the spread of the wavefunction itself at moderate field strengths (see the inset of Fig. 4d). The physical separation of the counterpropagating kink states can strongly suppress any type of valley-mixing mechanisms[27–30], and thus result in a robust topological protection of the kink states that resembles the picture of the chiral edge state in the quantum Hall effect.

What we demonstrate in this work—the creation of 1D topological conducting channels in BLG using electrical control—opens up exciting new avenues to implement valley-controlled valves, beam splitters and waveguides to control the electron flow in high-quality atomically thin materials[9,15]. Narrower junctions combined with the use of a larger bandgap can potentially enable the kink valleytronic devices to operate at non-cryogenic temperatures. The dual-split-gate structure demonstrated here will enable the realization of potential-controlled few-electron quantum dots[32] and open the door to the exploration of the fascinating edge-state and domain-wall physics in the quantum Hall regime of BLG[31,33].

Methods

Methods and any associated references are available in the online version of the paper.

References

1. Xiao, D., Chang, M.-C. & Niu, Q. Berry phase effects on electronic properties. *Rev. Mod. Phys.* **82,** 1959–2007 (2010).
2. Xu, X., Yao, W., Xiao, D. & Heinz, T. F. Spin and pseudospins in layered transition metal dichalcogenides. *Nat. Phys.* **10,** 343–350 (2014).
3. Rycerz, A., Tworzydlo, J. & Beenakker, C. W. J. Valley filter and valley valve in graphene. *Nat. Phys.* **3,** 172–175 (2007).
4. McCann, E. & Koshino, M. The electronic properties of bilayer graphene. *Rep. Prog. Phys.* **76,** 056503 (2013).
5. Zou, K. & Zhu, J. Transport in gapped bilayer graphene: the role of potential fluctuations. *Phys. Rev. B* **82,** 081407 (2010).
6. Martin, I., Blanter, Y. M. & Morpurgo, A. F. Topological confinement in bilayer graphene. *Phys. Rev. Lett.* **100,** 036804 (2008).
7. Li, J., Morpurgo, A. F., Büttiker, M. & Martin, I. Marginality of bulk-edge correspondence for single-valley Hamiltonians. *Phys. Rev. B* **82,** 245404 (2010).
8. Jung, J., Zhang, F., Qiao, Z. & MacDonald, A. H. Valley-Hall kink and edge states in multilayer graphene. *Phys. Rev. B* **84,** 075418 (2011).
9. Qiao, Z., Jung, J., Niu, Q. & MacDonald, A. H. Electronic highways in bilayer graphene. *Nano Lett.* **11,** 3453–3459 (2011).
10. Zarenia, M., Pereira, J. M. Jr, Farias, G. A. & Peeters, F. M. Chiral states in bilayer graphene: magnetic field dependence and gap opening. *Phys. Rev. B* **84,** 125451 (2011).
11. Zhang, F., MacDonald, A. H. & Mele, E. J. Valley Chern numbers and boundary modes in gapped bilayer graphene. *Proc. Natl Acad. Sci. USA* **110,** 10546–10551 (2013).
12. Alden, J. S. et al. Strain solitons and topological defects in bilayer graphene. *Proc. Natl Acad. Sci. USA* **110,** 11256–11260 (2013).
13. Vaezi, A., Liang, Y., Ngai, D. H., Yang, L. & Kim, E.-A. Topological edge states at a tilt boundary in gated multilayer graphene. *Phys. Rev. X* **3,** 021018 (2013).
14. Ju, L. et al. Topological valley transport at bilayer graphene domain walls. *Nature* **520,** 650–655 (2015).
15. Qiao, Z. et al. Current partition at topological channel intersections. *Phys. Rev. Lett.* **112,** 206601 (2014).
16. Yao, W., Xiao, D. & Niu, Q. Valley-dependent optoelectronics from inversion symmetry breaking. *Phys. Rev. B* **77,** 235406 (2008).
17. Mak, K. F., McGill, K. L., Park, J. & McEuen, P. L. The valley Hall effect in MoS₂ transistors. *Science* **344,** 1489–1492 (2014).
18. Gorbachev, R. V. et al. Detecting topological currents in graphene superlattices. *Science* **346,** 448–451 (2014).
19. Shimazaki, Y., Yamamoto, M., Borzenets, I. V., Watanabe, K., Taniguchi, T. & Tarucha, S. Generation and detection of pure valley current by electrically induced Berry curvature in bilayer graphene. *Nat. Phys.* **11,** 1032–1036 (2015).
20. Sui, M. et al. Gate-tunable topological valley transport in bilayer graphene. *Nat. Phys.* **11,** 1027–1031 (2015).
21. Li, J., Martin, I., Buttiker, M. & Morpurgo, A. F. Topological origin of subgap conductance in insulating bilayer graphene. *Nat. Phys.* **7,** 38–42 (2011).
22. Dean, C. R. et al. Boron nitride substrates for high-quality graphene electronics. *Nat. Nanotech.* **5,** 722–726 (2010).
23. Datta, S. *Electronic Transport in Mesoscopic Systems* (Cambridge Univ. Press, 1997).
24. Engels, S. et al. Limitations to carrier mobility and phase-coherent transport in bilayer graphene. *Phys. Rev. Lett.* **113,** 126801 (2014).
25. Stabile, A. A., Ferreira, A., Li, J., Peres, N. M. R. & Zhu, J. Electrically tunable resonant scattering in fluorinated bilayer graphene. *Phys. Rev. B* **92,** 121411 (2015).
26. Koenig, M. et al. Quantum spin Hall insulator state in HgTe quantum wells. *Science* **318,** 766–770 (2007).
27. Maciejko, J. et al. Kondo effect in the helical edge liquid of the quantum spin Hall state. *Phys. Rev. Lett.* **102,** 256803 (2009).
28. Law, K. T., Seng, C. Y., Lee, P. A. & Ng, T. K. Quantum dot in a two-dimensional topological insulator: the two-channel Kondo fixed point. *Phys. Rev. B* **81,** 041305 (2010).
29. Väyrynen, J. I., Goldstein, M. & Glazman, L. I. Helical edge resistance introduced by charge puddles. *Phys. Rev. Lett.* **110,** 216402 (2013).
30. Väyrynen, J. I., Goldstein, M., Gefen, Y. & Glazman, L. I. Resistance of helical edges formed in a semiconductor heterostructure. *Phys. Rev. B* **90,** 115309 (2014).
31. Mazio, V, Shimshoni, E, Huang, C.-W., Carr, S. T. & Fertig, H. A. Helical quantum Hall edge modes in bilayer graphene: a realization of quantum spin-ladders. *Phys. Scripta* **T165,** 014019 (2015).
32. Recher, P., Nilsson, J., Burkard, G. & Trauzettel, B. Bound states and magnetic field induced valley splitting in gate-tunable graphene quantum dots. *Phys. Rev. B* **79,** 085407 (2009).
33. Abanin, D. A. & Levitov, L. S. Quantized transport in graphene p–n junctions in a magnetic field. *Science* **317,** 641–643 (2007).
34. Zhu, J. Transport in bilayer and trilayer graphene: band gap engineering and band structure tuning. *APS March Meeting* http://meetings.aps.org/link/BAPS.2014.MAR.B30.1 (2014).

Acknowledgements

Author contributions

J.Z. and J.L. conceived the experiment. J.L. designed and fabricated the devices and made the measurements. K.J.M. assisted in optimizing the procedure used to fabricate the bottom split gates. J.L. and Z.Z. performed the COMSOL simulations. J.L. and J.Z. analysed the data. K. Wang, Y.R. and Z.Q. did the theoretical calculations. K. Watanabe and T.T. synthesized the h-BN crystals. J.L., J.Z., K. Wang, Y.R. and Z.Q. wrote the manuscript with input from all authors.

Additional information

Supplementary information is available in the online version of the paper. Reprints and permissions information is available online at www.nature.com/reprints. Correspondence and requests for materials should be addressed to J.Z. and Z.Q.

Competing financial interests

The authors declare no competing financial interests.

Methods

Device fabrication. The fabrication of the structure shown in Fig. 1c involved six steps. In step 1, we fabricated the bottom split gates made of multilayer graphene exfoliated from Kish graphite. Thin flakes (~2 nm) were exfoliated to SiO_2/doped Si substrates with 290 nm of thermal oxide. We used electron-beam lithography (EBL) and oxygen plasma etching (Plasma-Therm Versalock oxygen plasma 14 W power for about 30 s) to pattern the bottom split gate. Resist ZEP520A (300 $\mu C\ cm^{-2}$ dose, developed in n-amyl acetate, methyl isobutyl ketone/isopropyl alcohol (IPA) 8:1 and IPA at ~4 °C for 30 s each) was used as it provides better resolution than poly (methyl methacrylate) (PMMA). An example of a finished bottom split gate is shown in Supplementary Fig. 3a,b. The sample was then annealed in Ar/H_2 and/or treated in a very gentle oxygen plasma (MetroLine M4L) to remove ZEP residue. In step 2, thin flakes of h-BN (15–30 nm) and BLG were transferred sequentially to the bottom split gates using a PMMA/polyvinyl alcohol stamp[22]. In step 3, the BLG flake was shaped into a Hall bar with leads using standard EBL and oxygen plasma etching (Fig. 1c). In step 4, another thin flake of h-BN was transferred atop the stack to cover the Hall bar but not the graphene leads entirely. In step 5, standard EBL and metal deposition (5 nm Ti/70 nm Au) was used to make electrical contacts to the graphene leads. The resist was slightly overdeveloped to ensure good ohmic contacts. In step 6, we patterned the top split gates using EBL and metal deposition (5 nm Ti/ 20 nm Au). We measured the width of each pair of bottom split gates using SEM after ZEP removal. To obtain top split gates of matching width, we used empirical relations between the designed width and the actual width after exposure and lift-off; for example, a split designed to be 100 nm comes out to be around 70 nm because of the evaporation angle and the proximity effect of the electron-beam dose. Developing the top split-gate pattern in an ice bathed developer at ~4 °C (with a higher electron-beam dose of 450 $\mu C\ cm^{-2}$) provides better control of the development process and hence the dimension of the top split. Split widths w down to 50 nm can be made in this way, with higher yields for $w > 70$ nm because of occasional shorting along the splits. An example of the top split gates is shown in Supplementary Fig. 3c. To ensure the high quality of the sample, we annealed the h-BN top surfaces in Ar/O_2 (90/10%, 500 sccm (standard cubic centimetres per minute)) at 450 °C for 3 h and the graphene surfaces in Ar/H_2 (90/10%, 500 sccm) at 450 °C for 3 h before each transfer to remove the polymer residue from the previous transfer or lithography[35]. The layer-by-layer transfer approach ensures that both the top and bottom gates extend beyond the bilayer sheet, which creates a uniform density profile and ensures that the bulk of the bilayer becomes very insulating in the gapped regime. We avoided aligning the line junction with a straight flake edge that may suggest either the zigzag or the armchair orientation. The alignment of the top and bottom splits is critical to the success of the experiment. Although relying on the same pre-patterned alignment markers (made by a GCA 8000 stepper in our case, squares with 20 μm on the side) suffices for most multistep EBL fabrications that require alignment, the misalignment between the two pairs of split gates can be up to 90 nm in random directions even when an advanced electron-beam writer with a precise stage movement such as ours (Vistec EBPG5200) is used. The error primarily comes from the imperfection of the alignment markers made by optical lithography. We employed a realignment procedure to address this issue. In step 1 of the lithography, dummy graphene splits aligned with the bottom split gates were made (boxed area in Supplementary Fig. 4a). In step 5, when we patterned the Ti/Au electrodes, we also patterned metal splits designed to overlap with the dummy graphene splits, as shown in Supplementary Fig. 4b. In the same step, we wrote a second set of alignment markers designed to track the centre of the bottom split gates. As Supplementary Fig. 4c shows, the metal splits were slightly shifted from the dummy graphene splits (20 nm to the right in this case, but can be up to 90 nm). In step 6, in which we patterned the top split gates, we used the alignment markers made by EBL in step 5, which have more-precise dimensions, and made corrections for the misalignment determined in Supplementary Fig. 4c. As a final check, we made another pair of dummy metal splits concurrently with the top split gates in step 6. This is shown in Supplementary Fig. 4d. It was, indeed, aligned with the dummy graphene split underneath. Using this procedure, we can align the top and bottom split gates reliably to better than 10 nm. The width of the top and bottom split gates can be matched to better than 15 nm.

References

35. Garcia, A. G. F. *et al.* Effective cleaning of hexagonal boron nitride for graphene devices. *Nano Lett.* **12,** 4449–4454 (2012).